Mid-Infrared Slow Light Engineering and Tuning in 1-D Grating Waveguide

Yiming Ma, *Student Member, IEEE*, Bowei Dong, Bo Li, Jingxuan Wei, Yuhua Chang, Chong Pei Ho, and Chengkuo Lee, *Member, IEEE*

***Abstract*—The design, fabrication, and characterization of 1-D grating waveguide as slow light structure working in mid-infrared (MIR) region are demonstrated for the first time. The effects of various structural parameters on slow light properties are investigated through theoretical analysis, simulation and experimental verification, providing guidance on slow light engineering in 1-D grating waveguide. By adjusting structural parameters, average group indices of 9.4–15.5 with bandwidths of 23–66 nm and normalized delay-bandwidth products of 0.093–0.164 are obtained. Thermo-optic tuning is also demonstrated with π phase shift and group index tuning from 23 to 33 at the wavelength of 3.9024 μm by applying 1.4 mA current. The proposed tunable 1-D grating slow light waveguide provides a promising platform for various MIR applications such as on-chip absorption-based biochemical sensors, tunable optical buffers, and thermo-optic modulators.**

***Index Terms*—Slow light, gratings, optical waveguides, dispersion.**

I. INTRODUCTION

SILICON photonics (SiP) has attracted great research interest in past decades because it is a promising candidate to meet the dramatically increasing demands for high data transmission capacity in communication networks. The complementary metal-oxide-semiconductor (CMOS) compatibility of SiP enables low-cost and mass production of photonic devices. Numerous photonic devices have been demonstrated, most of which operate in near-infrared (NIR) C band and L band [1]–[7]. In fact, the NIR is not the only wavelength range where SiP can be utilized. Silicon (Si) is transparent up to the wavelength of about 8.5 μm, which extends to the mid-infrared (MIR) region [8]. Nowadays, MIR photonics has been attracting more and more attention because of its enormous potential in optical communications and label-free biochemical sensing. On the one hand, extending the optical bands from NIR to MIR is helpful in increasing the data transmission bandwidth of optical networks [9], [10]. On the other hand, for biochemical detection, MIR spectrum extensively overlaps with the functional group regions as well as fingerprint regions of various organic and inorganic compounds [11], [12].

In the MIR wavelength range, various fundamental building blocks, such as waveguide [13]–[17], microring resonator [13], multimode interference splitter (MMI) [13]–[15], Mach-Zehnder interferometer (MZI) [14], [15], directional coupler [15], [16], [18] and photonic crystal (PhC) cavity [19], have been demonstrated with good optical performance, establishing a solid foundation for MIR photonics applications. Thanks to the inherent high thermo-optic coefficient of Si, MIR modulators have been demonstrated by integrating spiral MZI with micro-heater [20]. MIR on-chip absorption-based biochemical sensors have also been realized using strip and slot waveguides [21]–[23]. Slow light with remarkably low group velocity offers the possibility for the spatial compression of optical energy, which reduces the device footprint and enhances light–matter interactions. Thus, slow light engineering is considered as one of the most promising techniques for improving the performance of optical modulators and sensors [24]–[33]. Slow light is also a feasible solution for buffering and various types of time-domain processing of optical signals. In addition, thermo-optic tuning of slow light devices enables advanced time-domain optical signal processing such as variable optical buffering and dynamic dispersion compensating [34]–[37].

Slow light on-chip can be realized using various periodic structures. One of the most commonly utilized is

Manuscript received January 31, 2018; revised March 13, 2018; accepted April 2, 2018. Date of publication April 16, 2018; date of current version May 18, 2018. This work was supported in part by the research grant of NRF-CRP15-2015-02 at the National University of Singapore (NUS), Singapore; in part by the research grant of NRF2015-NRF-ISF001-2620 at the NUS, Singapore; and in part by National Natural Science Foundation of China under Grant 61474078 at NUS (Suzhou) Research Institute, Suzhou, China. The work of Y. Ma was supported by NUS-NUSRI Research Scholarship. *(Corresponding author: Chengkuo Lee.)*

Y. Ma is with the NUS Suzhou Research Institute, Suzhou 215123 China, the Department of Electrical and Computer Engineering, National University of Singapore, Singapore 117576, Singapore, and also with the Center for Intelligent Sensors and MEMS, National University of Singapore, Singapore 117608, Singapore (e-mail: yimingma@u.nus.edu).

B. Dong is with the NUS Graduate School for Integrative Sciences and Engineering, Centre for Life Science, National University of Singapore, Singapore 117456, Singapore, the Department of Electrical and Computer Engineering, National University of Singapore, Singapore 117576, Singapore, and also with the Center for Intelligent Sensors and MEMS, National University of Singapore, Singapore 117608, Singapore (e-mail: dongbowei@u.nus.edu).

B. Li, J. Wei, and Y. Chang are with the Department of Electrical and Computer Engineering, National University of Singapore, Singapore 117576, Singapore, and also with the Center for Intelligent Sensors and MEMS, National University of Singapore, Singapore 117608, Singapore (e-mail: elelibo@nus.edu.sg; eleweij@nus.edu.sg; elecyu@nus.edu.sg).

C. P. Ho is with the Department of Electrical Engineering and Information Systems, The University of Tokyo, Tokyo 113-8656, Japan (e-mail: chongpei24@gmail.com).

C. Lee is with the NUS Suzhou Research Institute, Suzhou 215123, China, the Department of Electrical and Computer Engineering, National University of Singapore, Singapore 117576, Singapore, the Center for Intelligent Sensors and MEMS, National University of Singapore, Singapore 117608, Singapore, and also with the NUS Graduate School for Integrative Sciences and Engineering, Centre for Life Science, National University of Singapore, Singapore 117456, Singapore (e-mail: elelc@nus.edu.sg).

Color versions of one or more of the figures in this paper are available online at http://ieeexplore.ieee.org.

Digital Object Identifier 10.1109/JSTQE.2018.2827659

two-dimensional (2D) PhC waveguide [38]–[48]. 2D PhC waveguide has also been demonstrated in the MIR wavelength range and its slow light performance has been characterized. Although group index of 12 was achieved, the device was limited by narrow bandwidth (around 10 nm) resulted from large group velocity dispersion (GVD) [49]. This is a consequence of ignoring dispersion engineering, the purpose of which is to obtain a flat band away from the Brillouin zone (BZ) edge. Beside 2D PhC waveguide, one-dimensional (1D) grating waveguide has also been leveraged to realize slow light effect in NIR region [50]–[56]. These works reveal that 1D grating waveguide owns some critical advantages over 2D PhC waveguide. First, the simpler structure of 1D grating waveguide makes it easier to be fabricated and more impervious to fabrication imperfection than 2D PhC waveguide. Second, compared with 2D PhC waveguide, in 1D grating waveguide higher ratio of the optical power is confined in the cladding, leading to stronger light-matter interaction, which is conducive to biochemical sensing and nonlinear enhancement applications. Third, 1D grating waveguide has smaller lateral size compared with 2D PhC waveguide and thus has favorable potential for compact slow light devices. Nonetheless, the feasibility of adopting 1D grating waveguide for MIR slow light applications remains undiscovered. Besides, the influence of the structural parameters on the slow light effect based on 1D grating waveguide, which is important information for slow light design and engineering, has not been systematically investigated yet.

In this paper, we demonstrate for the first time, to the best of our knowledge, 1D grating waveguide with tunable flat band slow light effect in MIR region. The influence of the structural parameters of 1D grating waveguide on the slow light performance is firstly theoretically analyzed and numerically modeled using 2D plane wave expansion (PWE) method, and later verified through fabrication and characterization of numerous 1D grating waveguide slow light devices. Average group indices ranging from 9.4 to 15.5 with bandwidths of 23–166 nm are observed. Corresponding experimental normalized delay-bandwidth products (NDBPs) from 0.093 to 0.164 are comparable with those of reported 1D and 2D slow light structures operating in NIR region [39], [40], [47], [54]. The influence of 1D grating waveguide parameters not only serves as a design guideline for MIR slow light applications, but also is a general rule that could be utilized for applications at all other wavelengths based on such periodic structure. Additionally, thermo-optic tuning is also demonstrated using integrated micro-heaters. At the wavelength of 3.9024 μm, π phase shift and group index tuning from 23 to 33 are achieved with 1.4 mA applied current. The proposed tunable 1D grating slow light waveguide provides a promising platform for various MIR applications such as on-chip absorption-based biochemical sensors, tunable optical buffers and thermo-optic modulators.

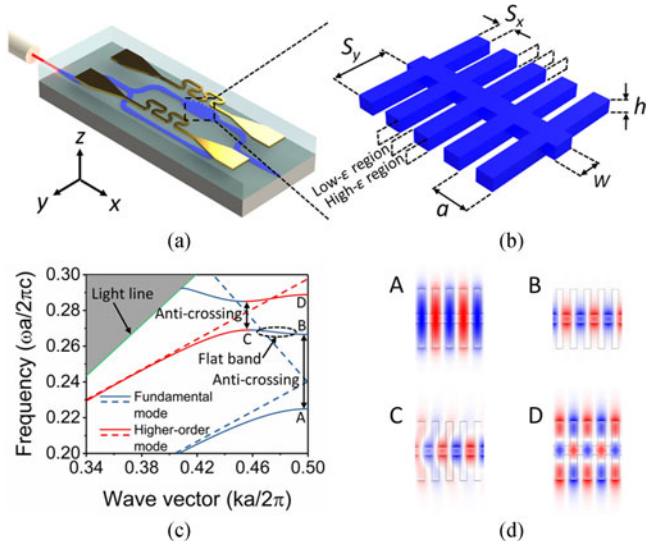

Fig. 1. (a) Schematic illustration of the slow light MZI integrated with micro-heaters. (b) Schematic illustration of the 1D grating waveguide. (c) Band diagram of the 1D grating waveguide with $S_x = 0.50a$, $S_y = 1.80a$ and $W = 0.60a$. (d) Mode profiles at the labelled points in (c).

II. Structure and Band Analysis

Fig. 1(a) shows the schematic structure of the proposed silicon-on-insulator (SOI) slow light device. A 1D grating waveguide with 303 periods is embedded into one arm (signal arm) of an MZI for the characterization of the slow light performance. The light from the input fiber is coupled into the device through an inversed tapered coupler with linearly broadened width from 0.3 μm to 1.2 μm over 200 μm length. The light then goes through an S band, which is utilized to stagger the input and output ports, making the alignment between fiber and waveguide easier. Thereafter, the light is divided equally into the two arms of the MZI by a Y-junction. On the signal arm, the waveguide width is linearly tapered down to the central waveguide width of the 1D grating waveguide and tapered back to 1.2 μm after passing though the 1D grating waveguide. To compensate for the mode mismatch and improve the coupling efficiency at the interface between the strip waveguide and the 1D grating waveguide, a tapered grating with linearly shortened grating teeth (number of periods $N = 6$) is utilized [50]. The only difference between the signal arm and the reference arm is the presence of grating teeth. Finally, the two light beams are recombined and output using a Y-junction and a tapered coupler of the same design as those at the input. On top of the upper silicon oxide (SiO_2) cladding layer, two identical micro-heaters are integrated with both arms of the MZI to realize thermo-optic tuning. The width of the micro-heater changes gradually between the pad and the resistance wire in order to avoid the saltation of electrical resistivity, which causes heat concentration and may burn out the micro-heater. The resistance wires are designed to be Ω-shape to distribute the heat more uniformly.

Fig. 1(b) schematically illustrates the 1D grating waveguide. The lattice constant a and thickness h of the 1D grating waveguide are fixed at 1.03 μm and 0.4 μm, respectively, to match the device working wavelengths with MIR region. The width and length of grating teeth are labelled as S_x and S_y, respectively, while the width of central waveguide is denoted as W. They are the main parameters to influence the band diagram [56]. The 1D grating waveguide is regarded as a periodic structure with alternating high-ε and low-ε regions, where ε is the effective dielectric constant. The high-ε region consists of the central waveguide and the long bilateral grating teeth while the low-ε region is composed of the central waveguide and the bilateral trench between two adjacent grating teeth, as indicated in Fig. 1(b). Since the 1D grating waveguide is accessed from single mode waveguide, transverse-electrical-like (TE-like) *y*-odd modes, which have even symmetry with respect to horizontal plane of symmetry $z = 0$ and odd symmetry with respect to vertical plane of symmetry $y = 0$, are most easily excited [52]. Therefore, only modes with these symmetries are taken into account in the band diagram. 2D simulation with a slab equivalent index of 2.44 for TE-like mode is adopted. The refractive index of SiO_2 is 1.40. Fig. 1(c) shows the calculated band diagram with $S_x = 0.50a$, $S_y = 1.80a$ and $W = 0.60a$. The dash lines in Fig. 1(c) presents the TE-like *y*-odd bands for the case of a nonperiodic waveguide. The fundamental mode (blue) is folded back at the first BZ edge, and therefore intersects with the higher-order mode (red) lying at a higher frequency. Considering the 1D grating waveguide, the structural periodicity allows the bands to couple to each other and then split at both the first BZ edge and the above-mentioned intersection point, which is known as anti-crossing effect [57], [58]. As a result, a hybrid band is formed, where the field pattern transforms continuously from the higher-order mode to the fundamental mode as wave vector *k* increases. Fig. 1(d) shows the mode profiles corresponding to the labelled points on Fig. 1(c). At the first BZ edge ($k = \pi/a$) where the modes have a wavelength of $2a$, exactly twice the lattice constant of the 1D grating waveguide, the low-frequency mode (point A) concentrates its energy in the high-ε regions, while the high-frequency mode (point B) has most of its energy localized in the low-ε regions. With decreasing *k*, the mismatch between the wavelength and the lattice constant becomes larger, thus the mode expands more into the adjacent high-ε region (point C). The higher-order mode (point D) has an additional pair of nodes and penetrates deeper into the periodic structure.

The behavior of the dispersion in the vicinity of both anti-crossing points B and C can be described using a simple parabolic approximation [59]:

$$\omega \approx \omega_0 \pm \left(\frac{\Delta k}{\alpha}\right)^2 \tag{1}$$

where ω is the mode frequency, ω_0 is the mode frequency at points B or C, Δk is the wave vector difference to its value at points B or C, α is positively related to the corrugation strength, which depends mostly on the index contrast and the structural parameters. From (1) it can be deduced that the stronger corrugation will lead to a flatter mode near the anti-crossing points. The first derivative over the wave vector *k* is the group velocity:

$$\nu_g = \frac{d\omega}{dk} \sim \frac{\Delta k}{\alpha^2} \sim \frac{(\omega - \omega_0)^{1/2}}{\alpha} \tag{2}$$

And the reciprocal of the group velocity v_g is the group index:

$$n_g = \frac{1}{v_g} \sim \frac{\alpha}{(\omega - \omega_0)^{1/2}} \tag{3}$$

We are interested in the S-shape dispersion band from point B to point C, whose profile can be conveniently engineered through adjusting the corrugation strength of the grating waveguide by designing S_x, S_y and *W* properly. A flat band away from the first BZ edge is obtained, which has nearly constant group velocity for a large bandwidth, as illustrated in Fig. 1(c).

The profile variation tendencies of the S-shape dispersion band BC with different structural parameters are theoretically studied with the aid of 2D simulation. Fig. 2(a) shows the band variation with S_x when S_y and *W* are fixed to be $1.80a$ and $0.60a$, respectively. To see the change of slope and frequency range more clearly, the bands corresponding to different values of S_x are moved to have their points B overlapped at the original location of point B of the band corresponding to $S_x = 0.50a$. The original results are shown in the inset. Fig. 2(b) shows the change tendency with regard to S_y with constant $S_x = 0.50a$ and $W = 0.60a$. Fig. 2(c) indicates the change tendency regarding *W* when S_x and S_y are fixed to be $0.50a$ and $1.80a$, respectively. Similar as Fig. 2(a), the bands corresponding to different values of *W* are moved to have their points B overlapped at the original location of point B of the band corresponding to $W = 0.60a$ for better presentation. The inset shows the original results. Fig. 2(d), (e) and (f) show the group indices versus wavelength extracted from the bands in Fig. 2(a), (b) and (c), respectively. These group index curves display the characteristics of U-shape with nearly constant group index over a large bandwidth. To be consistent with most of the previous works, here we evaluate the bandwidth as the wavelength range where group index variation of $\pm 10\%$ is tolerated [54].

Fig. 2(a)–(f) reveal that the band shifts to lower frequency, i.e., higher wavelength with either increasing S_x, S_y or *W*. This is because the ratio of mode field in the Si structure becomes higher, which increases the effective index. On contrary to S_x or *W* variation, the position of point B, i.e., the band edge, barely shifts with varying S_y, as shown in Fig. 2(b) and the insets of Fig. 2(a) and (c). This difference could be attributed to that the mode at point B interacts almost only with the bottom of the trench, as shown in Fig. 1(d) panel B, maintaining its effective index almost unchanged with varying S_y. To understand the change rules of the slope and the frequency range (in other words, the group index and the bandwidth) of the S-shape dispersion band BC, it is necessary to find out their potential link. First, point C shifts to larger *k* with increasing corrugation strength. This can be explained by that the slope of the higher-order mode experiences more drastic change than that of the fundamental mode since the previous is more sensitive to the change of corrugation strength due to its further penetration into the periodic structure, as indicated in Fig. 1(d) panel B and D. Second, as revealed in (1), band BC becomes flatter with stronger corrugation. Under the combined effect of point C shifting to larger k and the flattening of band BC, both the slope and the frequency range of band BC become smaller with stronger corrugation, revealing a trade-off between high group index and large bandwidth. The corrugation strength is increased with lengthening grating teeth, rising the group index and lowering the bandwidth, as shown in Fig. 2(b) and (e). With larger *W*, the widened central waveguide has better mode confinement, which deteriorates the

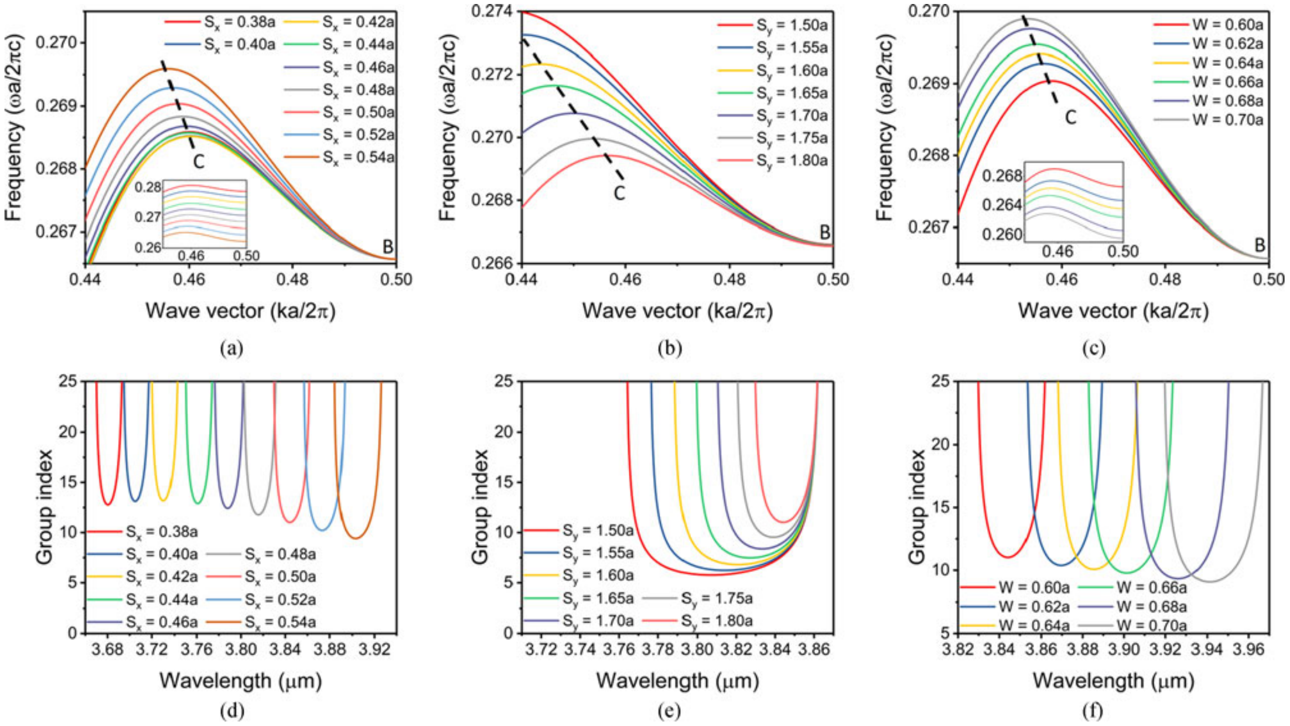

Fig. 2. (a) Dispersion band BC variation with S_x, when $S_y = 1.80a$ and $W = 0.60a$, all bands are moved to have their points B overlapped at the original location of point B of the band corresponding to $S_x = 0.50a$, the inset shows the original locations of the bands. (b) Dispersion band BC variation with S_y, when $S_x = 0.50a$ and $W = 0.60a$. (c) Dispersion band BC variation with W, when $S_x = 0.50a$ and $S_y = 1.80a$, all bands are moved to have their points B overlapped at the original location of point B of the band corresponding to $W = 0.60a$, the inset shows the original locations of the bands. (d), (e) & (f) Group index curves extracted from (a), (b) & (c), respectively.

corrugation, leading to contrary change tendency of group index and bandwidth to that with regard to S_y, as shown in Fig. 2(c) and (f). As for the variation with S_x, Fig. 2(a) and (d) indicate that the highest corrugation strength is achieved when S_x is equal to $0.42a$.

III. FABRICATION AND EXPERIMENT

The fabrication starts from a SOI wafer with 220 nm thick device layer and 2 μm thick buried oxide (BOX) layer. The device layer is epitaxially grown to 400 nm thick for MIR application. SiO_2 is deposited as the hard mask and patterned by deep ultraviolet (DUV) photolithography. The pattern is transferred to the Si device layer by reactive ion etching (RIE). 3 μm thick SiO_2 is then deposited, followed by chemical mechanical polishing (CMP) to obtain a planarized 2 μm thick upper cladding layer. Finally, 120 nm thick Titanium nitride (TiN) is deposited, patterned and etched to realize the micro-heater. TiN is chosen to be the micro-heater material because of its very high melting point (2930 °C), low electrical resistivity (20 $\mu\Omega\cdot$cm) and CMOS compatibility [60]. Fig. 3(a) shows the microscopic image of the fabricated devices with different dimensions of 1D grating waveguide. Limited by the space among MZIs, adjacent 4 or 5 MZIs share the same pair of electrical pads and the resistance wires above each signal arm of MZI are connected in series. Identical resistance wires are also arranged above every reference arm and connected in series to another pair of electrical pads. Consequently, the signal arm and the reference arm on each MZI can be heated independently. Fig. 3(b) and (c) show the zoom-in microscopic images of the 1D grating waveguide and the resistance wire, respectively. Fig. 3(d) shows the scanning electron microscope (SEM) image of the fabricated 1D grating waveguide.

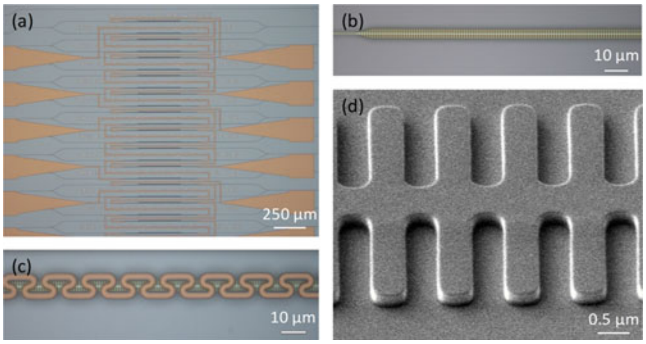

Fig. 3. (a) Microscopic image of the fabricated devices with different values of S_x, S_y and W. (b) Microscopic image of the 1D grating waveguide as well as the linear taper. (c) Microscopic image of the resistance wire. (d) SEM image of the 1D grating waveguide.

The measurement setup is shown in Fig. 4. The light source is a linearly polarized continuous wave tunable MIR laser (3.64–4.12 μm). A half wave plate is placed between the laser and the chopper for fine polarization control. The light is launched into the ZrF_4 MIR fiber using a fiber launch system equipped with a ZnSe focusing lens and is then butt coupled to the device fixed on the sample stage. Output light from the

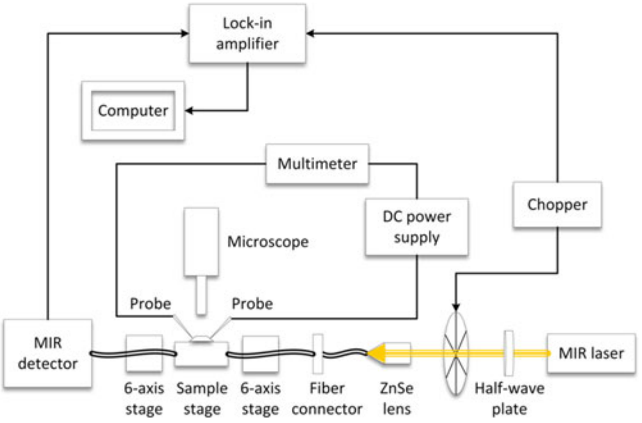

Fig. 4. Schematic illustration of measurement setup.

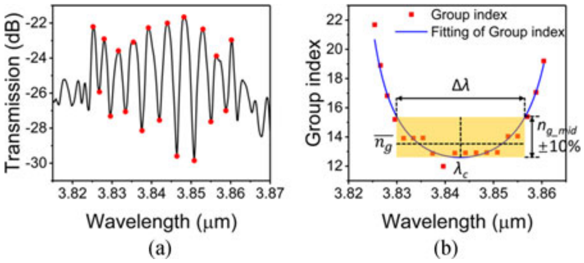

Fig. 5. (a) Measured transmission spectrum with $S_x = 0.50a$, $S_y = 1.80a$ and $W = 0.60a$. (b) Group index extracted from the spectrum in (a) and corresponding U-shape curve fitting. The bandwidth, average group index and NDBP are determined according to the fitting curve.

device is butt coupled to another MIR fiber and directed to the MIR detector which is connected to the lock-in amplifier for data reading. Both MIR fibers sit on the 6-axis stages to precisely control the alignment between them and the device. A vertical microscope above the sample sage is adopted to visualize the butt coupling condition. For realizing thermo-optic tuning, the two connected electrical pads are approached by probe tips simultaneously. The two probe stages are connected to the positive and negative ports of direct current (DC) power supply, respectively. A multimeter is connected in series into the circuit to measure the current.

Fig. 5(a) shows the transmission spectrum of a representative unbalanced MZI. The structural parameters of the 1D grating waveguide embedded into it are $S_x = 0.50a$, $S_y = 1.80a$ and $W = 0.60a$. The oscillation in the spectrum is due to the group velocity difference between the two arms of the MZI. The free spectral range (FSR) of the oscillation decreases near both anti-crossing points of the 1D grating waveguide, approximately 3.825 μm and 3.860 μm, corresponding to point C and point B, respectively. The group index therefore can be extracted from the oscillation pattern using the equation [34]:

$$n_g(\lambda) = n_g^{\mathrm{ref}}(\lambda) + \frac{\lambda_{\max}\lambda_{\min}}{2L\left|\lambda_{\max} - \lambda_{\min}\right|} \quad (4)$$

where n_g is the group index of the 1D grating waveguide, n_g^{ref} is the group index of the reference strip waveguide with slight wavelength dependence and is extracted from 2D finite element method (FEM) calculated dispersion relation, $\lambda_{\max}$ and $\lambda_{\min}$ are the wavelengths at adjacent valley and peak of the oscillation, and L represents the length of the 1D grating waveguide. The extracted group indices are plotted in Fig. 5(b). As suggested by (3), negative one-half time-squares fitting is adopted near both anti-crossing points to realize the U-shape curve fitting. The measured bandwidth $\Delta\lambda$ is determined according to the fitting curve, as illustrated in Fig. 5(b). The NDBP is a good indication of the highest slow light capacity that the device potentially provides and is defined as [42]:

$$\mathrm{NDBP} = \frac{\overline{n_g} \times \Delta\lambda}{\lambda_c} \quad (5)$$

where λ_c is the central wavelength of the flat band slow light region, $\overline{n_g}$ is the average group index calculated by:

$$\overline{n_g} = \int_{\lambda_c - \Delta\lambda/2}^{\lambda_c + \Delta\lambda/2} n_g(\lambda)\, d\lambda / \Delta\lambda \quad (6)$$

1D grating waveguides with varying S_x, S_y and W are measured. The measured group indices and corresponding fittings are shown in Fig. 6(a), (b) and (c). The highest measurable group index is limited by the wavelength accuracy of the MIR laser as well as the residual Fabry–Perot (FP) noise that arises from interference in the optical circuit outside the MZI. Close to both anti-crossing points, the amplitude and FSR of the oscillation become ambiguous because it is comparable with that of the FP noise [34]. Fig. 6(a) shows the dependence of the slow light performance on S_x. The highest group index as well as the narrowest bandwidth appear at $S_x = 0.44a$, which is slightly larger than the simulated value $0.42a$. This might be mainly caused by the fabrication imperfection. As shown in Fig. 3(d), the designed square corners become rounded in fabricated devices due to the limitation of the 248-nm lithographer. These rounded corners narrow the gap between the effective indices of the alternating high-ε and low-ε regions, which are noted as n_h and n_l, respectively. For 1D periodic structures, it is known that the corrugation strength reaches its maximum at [58]:

$$n_h S_x = n_l\left(a - S_x\right) \quad (7)$$

Therefore, the experimental extreme value of S_x is closer to $0.50a$ than the simulated one. Except this quantitative mismatch, all the change tendencies obtained in the measurement qualitatively agree well with those revealed by theoretical analysis and simulation, which provides a solid guideline on the slow light engineering in the 1D grating waveguide through adjusting the structural parameters. By altering structural parameters, average group indices of 9.4–15.5 with bandwidths of 23–66 nm are obtained. Corresponding NDBPs are calculated to be from 0.093 to 0.164, which are comparable with those of reported 1D and 2D slow light structures operating in NIR region [39], [40], [47], [54]. The NDBP increases when average group index decreases, which is due to that the corresponding bandwidth increases more rapidly. This tendency is similar to that in 2D PhC waveguide [42], [44]. The sensitivities of slow light properties with structural parameters are determined by the slopes of corresponding linear fittings. For the sensitivities with S_x, monotone

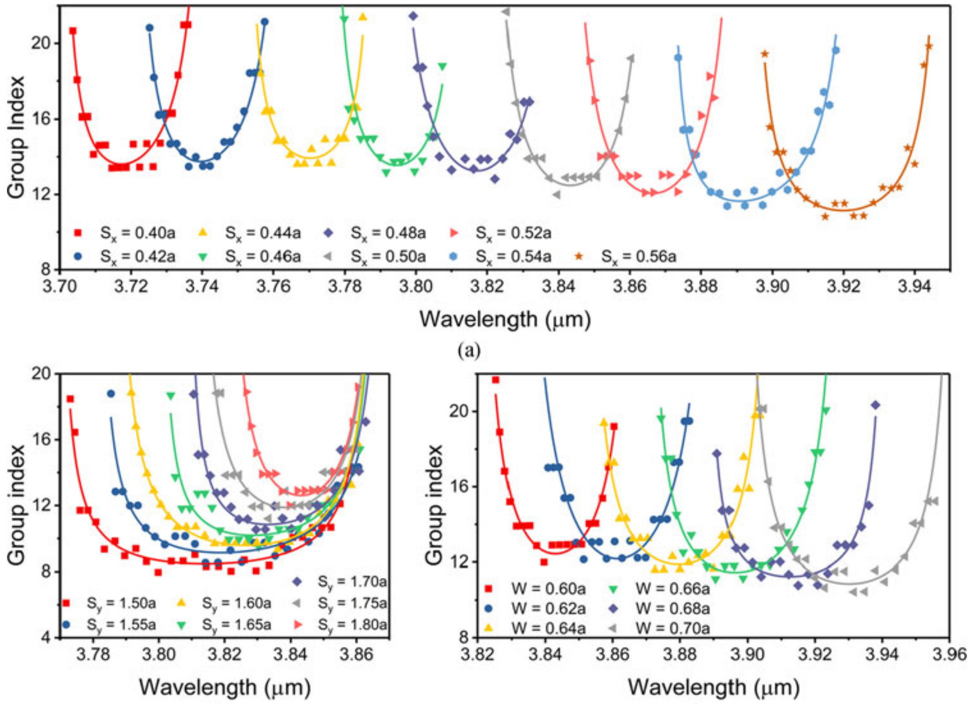

(a)

(b)

(c)

Fig. 6. Group index curve variation with (a) S_x, when $S_y = 1.80a$ and $W = 0.60a$; (b) S_y, when $S_x = 0.50a$ and $W = 0.60a$; (c) W, when $S_x = 0.50a$ and $S_y = 1.80a$.

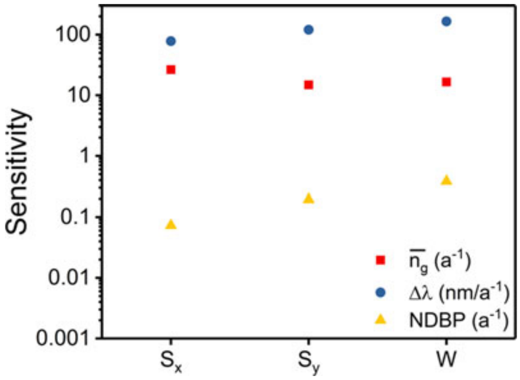

Fig. 7. Summarized plot of the sensitivities of slow light properties with structural parameters.

interval of $[0.44a, 0.54a]$ is selected for the characterization. All extracted sensitivities are plotted together in Fig. 7. It is seen that S_x is the most sensitive parameter to change the average group index, while W is the most sensitive one with respect to the bandwidth and the NDBP. Although S_y is not as sensitive as S_x and W, its variation range can be larger, leading to wider tuning ranges of slow light properties. The feasible largest and smallest S_x are strongly limited by the critical dimension of the fabrication capability. Likewise, W needs a moderate value considering the issues of mode confinement and propagation loss. Besides, S_y is the most appropriate parameter to be engineered when large-scale adjustment of slow light properties without significant influence on the wavelength, especially the band edge, is required. On the contrary, S_x has the highest priority when considering large tuning range of the wavelength, as shown in Fig. 6(a), (b) and (c). The position of the band edge, where the slow light effect reaches the strongest, is required to be carefully engineered for various applications. While utilizing slow light structures for absorption sensing, for example, it is best to locate the band edge as close as possible to the absorption peak of the analyte in order to enhance the detection sensitivity [32].

1D grating waveguide with $S_x = 0.50a$, $S_y = 1.80a$ and $W = 0.70a$ is used for the demonstration of thermo-optic tuning. Fig. 8(a) shows the measured transmission spectra with different current levels applied to the signal and reference arms. The spectra are manually shifted vertically by 4 dB for clarity. As expected, heating of the reference arm (with its group index nearly constant throughout this spectral region) does not result in significant changes of the measured transmission spectrum. On the contrary, heating of the signal arm results in the wavelength shift of the interference signal to longer wavelengths. With 0.7 mA applied current, the interference signal shifts only about 0.4 nm. When the current is increased to 1.4 mA, more drastic shift of around 1.2 nm is observed. At the wavelength of 3.9024 μm, applying 1.4 mA current on the signal arm results in almost π phase shift, as marked by the black dash line. The group indices of the 1D grating waveguide with 0 and 1.4 mA applied current on the signal arm are deduced and fitted using the procedure described above, as shown in Fig. 8(b). It is seen that the derived group index curve almost maintains its shape yet shifts to longer wavelengths with increasing applied current, indicating both the average group index and the bandwidth almost remain unchanged. However, at some specific wavelengths, the

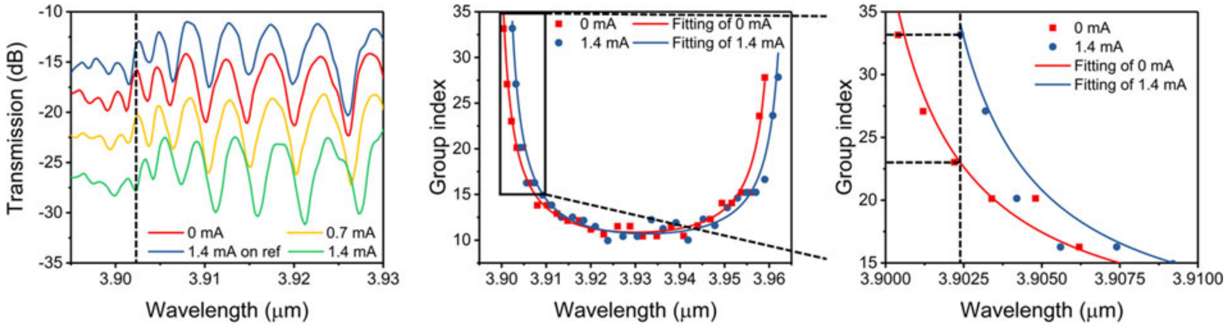

(a) (b) (c)

Fig. 8. (a) Measured transmission spectra with different applied current. Spectra are manually shifted vertically by 4 dB for clarity. Red, blue, yellow and green spectra correspond to zero applied current, 1.4 mA current applied to the reference arm, 0.7 mA and 1.4 mA current applied to the signal arm, respectively. (b) Group index curves corresponding to 0 and 1.4 mA current applied to the signal arm. (c) Zoom-in of the zone indicated by the black square box in (b).

group index can be significantly tuned. At 3.9024 μm, the group index is tuned from 23 to 33 with 1.4 mA current applied on the signal arm, as shown in Fig. 8(c). An even larger tuning range of phase and group index can be achieved at wavelengths closer to the anti-crossing points, where the slow light effect is stronger.

IV. CONCLUSION

In conclusion, we experimentally demonstrated the first 1D grating waveguide with tunable flat band slow light effect in MIR region. The influence of various structural parameters on slow light properties was studied through theoretical analysis, simulation and experimental verification. The experimental results are consistent with our theoretical prediction and simulation, providing a solid guideline on the design of 1D grating slow light waveguide for not only MIR applications, but also applications at all other wavelengths based on such periodic structure. By altering structural parameters, average group indices of 9.4–15.5 with bandwidths of 23–66 nm are achieved. Corresponding NDBPs of 0.093–0.164 are comparable with those of reported 1D and 2D NIR slow light structures. As a promising method for realizing active control of slow light performance, thermo-optic tuning was also demonstrated in 1D grating waveguide. π phase shift and group index tuning from 23 to 33 were achieved at 3.9024 μm with 1.4 mA applied current. Our results can be adopted in the realization of MIR slow light for various applications such as on-chip absorption-based biochemical sensors, tunable optical buffers and thermo-optic modulators.

REFERENCES

[1] R. Soref, "The past, present, and future of silicon photonics," *IEEE J. Sel. Topics Quantum Electron.*, vol. 12, no. 6, pp. 1678–1687, Nov./Dec. 2006.

[2] B. Jalali and S. Fathpour, "Silicon photonics," *J. Lightw. Technol.*, vol. 24, no. 12, pp. 4600–4615, Dec. 2006.

[3] B. L. Tsybeskov and D. J. Lockwood, "Silicon photonics: CMOS going optical," *Proc. IEEE*, vol. 97, no. 7, pp. 1161–1165, Jul. 2009.

[4] B. Li and C. Lee, "NEMS diaphragm sensors integrated with triple-nano-ring resonator," *Sens. Actuators A, Phys.*, vol. 172, no. 1, pp. 61–68, 2011.

[5] B. Li, F. L. Hsiao, and C. Lee, "Configuration analysis of sensing element for photonic crystal based NEMS cantilever using dual nano-ring resonator," *Sens. Actuators A, Phys.*, vol. 169, no. 2, pp. 352–361, 2011.

[6] B. Li, F. L. Hsiao, and C. Lee, "Computational characterization of a photonic crystal cantilever sensor using a hexagonal dual-nanoring-based channel drop filter," *IEEE Trans. Nanotechnol.*, vol. 10, no. 4, pp. 789–796, Jul. 2011.

[7] C. P. Ho, B. Li, A. J. Danner, and C. Lee, "Design and modeling of 2-D photonic crystals based hexagonal triple-nano-ring resonators as biosensors," *Microsyst. Technol.*, vol. 19, no. 1, pp. 53–60, 2013.

[8] R. Soref, "Mid-infrared photonics in silicon and germanium," *Nature Photon.*, vol. 4, no. 8, pp. 495–497, 2010.

[9] X. Liu *et al.*, "Bridging the mid-infrared-to-telecom gap with silicon nanophotonic spectral translation," *Nature Photon.*, vol. 6, no. 10, pp. 667–671, 2012.

[10] A. Schliesser, N. Picqué, and T. W. Hänsch, "Mid-infrared frequency combs," *Nature Photon.*, vol. 6, no. 7, pp. 440–449, 2012.

[11] V. M. Lavchiev and B. Jakoby, "Photonics in the mid-infrared: Challenges in single-chip integration and absorption sensing," *IEEE J. Sel. Topics Quantum Electron.*, vol. 23, no. 2, Mar./Apr. 2017, Art. no. 8200612.

[12] T. Hu *et al.*, "Silicon photonic platforms for mid-infrared applications," *Photon. Res.*, vol. 5, no. 5, pp. 417–430, 2017.

[13] M. M. Milošević *et al.*, "Silicon waveguides and devices for the mid-infrared," *Appl. Phys. Lett.*, vol. 101, no. 12, 2012, Art. no. 121105.

[14] M. Nedeljkovic *et al.*, "Silicon photonic devices and platforms for the mid-infrared," *Opt. Mater. Express*, vol. 3, no. 9, pp. 1205–1214, 2013.

[15] G. Z. Mashanovich *et al.*, "Silicon photonic waveguides and devices for near- and mid-IR applications," *IEEE J. Sel. Topics Quantum Electron.*, vol. 21, no. 4, Jul./Aug. 2015, Art. no. 8200112.

[16] B. Dong *et al.*, "Silicon-on-insulator waveguide devices for broadband mid-infrared photonics," *IEEE Photon. J.*, vol. 9, no. 3, Jun. 2017, Art. no. 4501410.

[17] R. Gamal, Y. Ismail, and M. Swillam, "Silicon waveguides at the mid-infrared," *J. Lightw. Technol.*, vol. 33, no. 15, pp. 3207–3214, Aug. 2015.

[18] B. Dong *et al.*, "Compact low loss mid-infrared wavelength-flattened directional coupler (WFDC) for arbitrary power splitting ratio enabled by rib waveguide dispersion engineering," *IEEE J. Sel. Topics Quantum Electron.*, vol. 24, no. 4, Jul./Aug. 2018, Art. no. 4500108, doi: 10.1109/JSTQE.2018.2811902.

[19] R. Shankar, I. Bulu, R. Leijssen, and M. Lončar, "Study of thermally-induced optical bistability and the role of surface treatments in Si-based mid-infrared photonic crystal cavities," *Opt. Express*, vol. 19, no. 24, pp. 24828–24837, 2011.

[20] M. Nedeljkovic *et al.*, "Mid-infrared thermo-optic modulators in SoI," *IEEE Photon. Technol. Lett.*, vol. 26, no. 13, pp. 1352–1355, Jul. 2014.

[21] P. T. Lin *et al.*, "Chip-scale mid-infrared chemical sensors using air-clad pedestal silicon waveguides," *Lab Chip*, vol. 13, no. 11, pp. 2161–2166, 2013.

[22] P. T. Lin *et al.*, "Mid-infrared spectrometer using opto-nano fluidic slot-waveguide for label-free on-chip chemical sensing," *Nano Lett.*, vol. 14, no. 1, pp. 231–238, 2014.

[23] W. Zhou *et al.*, "Fully suspended slot waveguides for high refractive index sensitivity," *Opt. Lett.*, vol. 42, no. 7, pp. 1245–1248, 2017.

[24] T. Baba, "Slow light in photonic crystals," *Nature Photon.*, vol. 2, no. 8, pp. 465–473, 2008.

[25] A. Brimont, P. Sanchis, and J. Martí, "Strong electro-optical modulation enhancement in a slow wave corrugated waveguide," *Opt. Express*, vol. 17, no. 11, pp. 9204–9211, 2009.

[26] C. Y. Lin *et al.*, "Electro-optic polymer infiltrated silicon photonic crystal slot waveguide modulator with 23 dB slow light enhancement," *Appl. Phys. Lett.*, vol. 97, no. 9, 2010, Art. no. 93304.

[27] X. Wang *et al.*, "Effective in-device r_33 of 735 pm/V on electro-optic polymer infiltrated silicon photonic crystal slot waveguides," *Opt. Lett.*, vol. 36, no. 6, pp. 882–884, 2011.

[28] S. Inoue and A. Otomo, "Electro-optic polymer/silicon hybrid slow light modulator based on one-dimensional photonic crystal waveguides," *Appl. Phys. Lett.*, vol. 103, no. 17, 2013, Art. no. 171101.

[29] H. Yan *et al.*, "One-dimensional photonic crystal slot waveguide for silicon-organic hybrid electro-optic modulators," *Opt. Lett.*, vol. 41, no. 23, pp. 5466–5469, 2016.

[30] J. García-Rupérez *et al.*, "Label-free antibody detection using band edge fringes in SOI planar photonic crystal waveguides in the slow-light regime," *Opt. Express*, vol. 18, no. 23, pp. 24276–24286, 2010.

[31] W. C. Lai, S. Chakravarty, X. Wang, C. Lin, and R. T. Chen, "Photonic crystal slot waveguide absorption spectrometer for on-chip near-infrared spectroscopy of xylene in water," *Appl. Phys. Lett.*, vol. 98, no. 2, 2011, Art. no. 23304.

[32] W.-C. Lai, S. Chakravarty, X. Wang, C. Lin, and R. T. Chen, "On-chip methane sensing by near-IR absorption signatures in a photonic crystal slot waveguide," *Opt. Lett.*, vol. 36, no. 6, pp. 984–986, 2011.

[33] K. Qin, S. Hu, S. T. Retterer, I. I. Kravchenko, and S. M. Weiss, "Slow light Mach–Zehnder interferometer as label-free biosensor with scalable sensitivity," *Opt. Lett.*, vol. 41, no. 4, pp. 753–756, 2016.

[34] Y. A. Vlasov, M. O'Boyle, H. F. Hamann, and S. J. McNab, "Active control of slow light on a chip with photonic crystal waveguides," *Nature*, vol. 438, no. 7064, pp. 65–69, 2005.

[35] N. Ishikura, T. Baba, E. Kuramochi, and M. Notomi, "Large tunable fractional delay of slow light pulse and its application to fast optical correlator," *Opt. Express*, vol. 19, no. 24, pp. 24102–24108, 2011.

[36] F. Shinobu, N. Ishikura, Y. Arita, T. Tamanuki, and T. Baba, "Continuously tunable slow-light device consisting of heater-controlled silicon microring array," *Opt. Express*, vol. 19, no. 14, 2011, Art. no. 13557.

[37] N. Ishikura, R. Hosoi, R. Hayakawa, T. Tamanuki, and M. Shinkawa, "Photonic crystal tunable slow light device integrated with multi-heaters," *Appl. Phys. Lett.*, vol. 100, no. 22, 2012, Art. no. 221110.

[38] M. Li *et al.*, "Harnessing optical forces in integrated photonic circuits," *Nature*, vol. 456, no. 7221, pp. 480–484, 2008.

[39] Y. Hamachi, S. Kubo, and T. Baba, "Slow light with low dispersion and nonlinear enhancement in a lattice-shifted photonic crystal waveguide," *Opt. Lett.*, vol. 34, no. 7, pp. 1072–1074, 2009.

[40] J. Jágerská *et al.*, "Experimental observation of slow mode dispersion in photonic crystal coupled-cavity waveguides," *Opt. Lett.*, vol. 34, no. 3, pp. 1546–1548, 2009.

[41] J. Hou, D. Gao, H. Wu, R. Hao, and Z. Zhou, "Flat band slow light in symmetric line defect photonic crystal waveguides," *IEEE Photon. Technol. Lett.*, vol. 21, no. 20, pp. 1571–1573, Oct. 2009.

[42] R. Hao *et al.*, "Novel slow light waveguide with controllable delay-bandwidth product and ultra-low dispersion," *Opt. Express*, vol. 18, no. 6, pp. 5942–5950, 2010.

[43] R. Hao *et al.*, "Improvement of delay-bandwidth product in photonic crystal slow-light waveguides," *Opt. Express*, vol. 18, no. 16, pp. 16309–16319, 2010.

[44] R. Hao *et al.*, "Novel kind of semislow light photonic crystal waveguides with large delay-bandwidth product," *IEEE Photon. Technol. Lett.*, vol. 22, no. 11, pp. 844–846, Jun. 2010.

[45] M. Ebnali-Heidari, C. Grillet, C. Monat, and B. J. Eggleton, "Dispersion engineering of slow light photonic crystal waveguides using microfluidic infiltration," *Opt. Express*, vol. 17, no. 3, pp. 1628–1635, 2009.

[46] B. Li, C. P. Ho, F.-L. Hsiao, and C. Lee, "Lateral lattice shift engineered slow light in elliptical photonics crystal waveguides," *J. Nanophoton.*, vol. 8, no. 1, 2014, Art. no. 84090.

[47] S. Serna *et al.*, "Experimental GVD engineering in slow light slot photonic crystal waveguides," *Sci. Rep.*, vol. 6, pp. 1–9, 2016.

[48] J. Li, L. O'Faolain, I. H. Rey, and T. F. Krauss, "Four-wave mixing in photonic crystal waveguides: Slow light enhancement and limitations," *Opt. Express*, vol. 19, no. 5, pp. 4458–4463, 2011.

[49] C. Reimer *et al.*, "Mid-infrared photonic crystal waveguides in silicon," *Opt. Express*, vol. 20, no. 28, pp. 29361–29368, 2012.

[50] M. L. Povinelli, S. G. Johnson, and J. D. Joannopoulos, "Slow-light, band-edge waveguides for tunable time delays," *Opt. Express*, vol. 13, no. 18, pp. 7145–7159, 2005.

[51] F. Riboli, P. Bettotti, and L. Pavesi, "Band gap characterization and slow light effects in one dimensional photonic crystals based on silicon slot-waveguides," *Opt. Express*, vol. 15, no. 19, pp. 11769–11775, 2007.

[52] J. Garcia, P. Sanchis, A. Martinez, and J. Marti, "1D periodic structures for slow-wave induced non-linearity enhancement," *Opt. Express*, vol. 16, no. 5, pp. 3146–3160, 2008.

[53] D. Gao *et al.*, "Wideband slow light in one-dimensional chirped holey grating waveguide," *IEEE Photon. Technol. Lett.*, vol. 22, no. 15, pp. 1135–1137, Aug. 2010.

[54] A. Brimont, A. Griol, J. Martí, and P. Sanchis, "Group index engineering in silicon corrugated waveguides," *Opt. Lett.*, vol. 35, no. 16, pp. 2708–2710, 2010.

[55] C. Bao *et al.*, "Low dispersion slow light in slot waveguide grating," *IEEE Photon. Technol. Lett.*, vol. 23, no. 22, pp. 1700–1702, Nov. 2011.

[56] C. Bao *et al.*, "Flat band slow light with high coupling efficiency in one-dimensional grating waveguides," *IEEE Photon. Technol. Lett.*, vol. 24, no. 1, pp. 7–9, Jan. 2012.

[57] O. Khayam and H. Benisty, "General recipe for flatbands in photonic crystal waveguides," *Opt. Express*, vol. 17, no. 17, pp. 14634–14648, 2009.

[58] J. J. D. Joannopoulos, S. Johnson, J. N. J. Winn, and R. R. D. Meade, *Photonic Crystals: Molding the Flow of Light*. Princeton, NJ, USA: Princeton Univ. Press, 2008.

[59] A. Petrov, "Slow light photonic crystal line-defect waveguides," Doctoral dissertation, Inst. Opt. Electron. Mater., Hamburg Univ. Technol., Hamburg, Germany, 2008.

[60] J. F. Creemer *et al.*, "Microhotplates with TiN heaters," *Sens. Actuators A, Phys.*, vol. 148, no. 2, pp. 416–421, 2008.

Yiming Ma (S'18) received the B.Eng. degree in mechatronics engineering from the School of Mechanical Engineering, Zhejiang University, Hangzhou, China, in 2016, and is currently working toward the Ph.D. degree in the Department of Electrical and Computer Engineering, National University of Singapore, Singapore. His research interests focus mainly on nanophotonics and its integration with MEMS for sensing applications.

Bowei Dong received the B.S. degree in physics with second major in mathematics from Nanyang Technological University, Singapore, in 2015, and is currently working toward the Ph.D. degree at the National University of Singapore, Singapore. His research interests include waveguides, integrated silicon photonics, and integrated mid-infrared photonics for sensing and healthcare applications.

Bo Li received the B.Eng. and Ph.D. degrees from the Department of Electrical and Computer Engineering, National University of Singapore, in 2009 and 2013, respectively. His research interests include nanophotonics and its integration with MEMS for sensing applications.

Jingxuan Wei received the B.S. degree from the Department of Physics, Nanjing University, China, in 2013, the M.Sc. degree from the Abbe School of Photonics, Friedrich-Schiller-University Jena, Germany, in 2016, and is currently working toward the Ph.D. degree in the Department of Electrical and Computer Engineering, National University of Singapore, Singapore. His research interests focus mainly on hybrid plasmonic-photonic devices with potential applications in sensing and integrated photonics.

Yuhua Chang received the B.S. degree from the School of Optical and Electronic Information, Huazhong University of Science and Technology, China, in 2016, and is currently working toward the Ph.D. degree in the Department of Electrical and Computer Engineering, National University of Singapore, Singapore. His research interests focus mainly on Si/AlN based IR photonics for sensing application.

Chong Pei Ho received the B.Eng. and Ph.D. degrees from the Department of Electrical and Computer Engineering, National University of Singapore, in 2011 and 2016, respectively. He continued his affiliation with the university as a research fellow until 2017. He moved on to the University of Tokyo after he was awarded the Overseas Research Fellowship by Japan Society for the Promotion of Science. His research interests include nanophotonics, optics and integration of these technologies with MEMS.

Chengkuo Lee (S'93–M'96) is the Director of Center for Intelligent Sensors and MEMS at National University of Singapore. He received the M.Sc. degree from Department of Materials Science and Engineer, National Tsing Hua University, Hsinchu, Taiwan, in 1991, M.Sc. degree from the Department of Industrial and System Engineering, the State University of New Jersey, Brunswick, NJ, USA, in 1993, and the Ph.D. degree from the Department of Precision Engineering, University of Tokyo, Tokyo, Japan, in 1996. His research interest include energy harvesting, nanophotonics, and MEMS.